

Bipolar Covalent Organic Framework Membranes

Engineering Bipolar Covalent Organic Framework Membranes for Selective Acid Extraction

Di Wu⁺, Zhiwei Xing⁺, Qing Guo, Zhuozhi Lai, Jiaming Yi, Qing-Wei Meng, Sai Wang, Zhifeng Dai, Shengqian Ma, and Qi Sun*

Abstract: Nitric acid (HNO₃) is a vital industrial chemical, and its recovery from complex waste streams is essential for sustainability and resource optimization. This study demonstrates the effectiveness of bipolar covalent organic framework (COF) membranes with tunable ionic site distributions as a solution for this challenge. The membranes are fabricated by layering anionic COF nanosheets on cationic COF layers, supported by a porous substrate. The resulting membranes exhibit significant rectifying behavior, driven by the asymmetric charge polarity and the intrinsic electric field, which enhances HNO₃ transport. The transmembrane diffusion coefficient of $2.74 \times 10^{-5} \text{ cm}^2 \text{ s}^{-1}$ exceeds the self-diffusion rate of NO₃⁻, leading to increased HNO₃ flux and selectivity compared to the individual anionic and cationic COF membranes. The optimized bipolar membrane configuration achieves remarkable separation factors, ranging from 22 to 242,000 for HNO₃, in comparison to other solutes such as HCl, H₂SO₄, H₃PO₄, and various metal salts in an eight-component mixed waste stream. This results in a substantial increase in HNO₃ purity, from 12.5% to 94.1% after a single membrane separation. With the broad range of COF materials and the versatility of the proposed membrane design, this work represents a significant advancement in chemical separation technologies.

Introduction

The development of energy-efficient ion-selective separation technologies is a critical frontier in sustainable resource recovery, particularly for extracting high-value ions from complex industrial effluents and natural brines.^[1–6] Although ion-selective membranes have shown considerable promise for high-performance separations,^[7–25] traditional methods based solely on size exclusion or static charge mechanisms face inherent limitations when distinguishing ions with similar hydration radii or valence states.^[26] This technological gap underscores the contrast with biological ion channels,

which achieve atomic-level precision through angstrom-scale selectivity filters. These filters mainly operate through two synergistic mechanisms: i) geometrically confined ionic moieties, surrounded by electrically neutral residues, facilitate ion-specific recognition through a combination of electrostatic interactions and short-range forces (e.g., ion-dipole coordination and hydrogen bonding);^[27–30] ii) asymmetric architectures with charge polarity asymmetry establish rectified ion transport pathways, thereby enhancing both selectivity and flux density.^[31–36] These biological principles have inspired the design of artificial membranes capable of programmable ion discrimination (Figure 1a).

Covalent organic frameworks (COFs), with their crystalline porosity and tunable synthesis, have recently emerged as promising biomimetic platforms for ion-selective separation.^[37–48] The periodic arrangement of functional groups within COF nanochannels mirrors the precise structure of biological selectivity filters. By strategically incorporating ionic building blocks via specific linkages, such as β -ketoenamine, COFs can replicate the short-range interaction chemistry found in protein-based charged filters, thus enhancing ion recognition.^[49,50] However, fabricating COF membranes with polarity-driven asymmetric charge distributions presents significant challenges. Although the dynamic nature of covalent bonds in COFs enables self-healing via dissolution-recrystallization processes, it also raises concerns about stability during multilayer fabrication. The deposition of additional COF layers may induce linker exchange or partial dissolution of the underlying structure, potentially compromising the integrity of the membrane.^[51,52] Although many ionic COFs can be converted into nanosheets and assembled into bipolar COF membranes via


[*] D. Wu⁺, Z. Xing⁺, Q. Guo, Z. Lai, J. Yi, Q.-W. Meng, Q. Sun
Zhejiang Provincial Key Laboratory of Advanced Chemical
Engineering Manufacture Technology, College of Chemical and
Biological Engineering, Zhejiang University, Hangzhou 310058,
China
E-mail: sunqichs@zju.edu.cn

S. Wang
Hangzhou Institute of Advanced Studies, Zhejiang Normal
University, Hangzhou 310015, China

Z. Dai
Key Laboratory of Surface & Interface Science of Polymer Materials
of Zhejiang Province, School of Chemistry and Chemical
Engineering, Zhejiang Sci-Tech University, Hangzhou 310018, China

S. Ma
Department of Chemistry, University of North Texas, 1508 W
Mulberry St, Denton, Texas 76201, USA

[⁺] Both authors contributed equally to this work.

 Additional supporting information can be found online in the
Supporting Information section

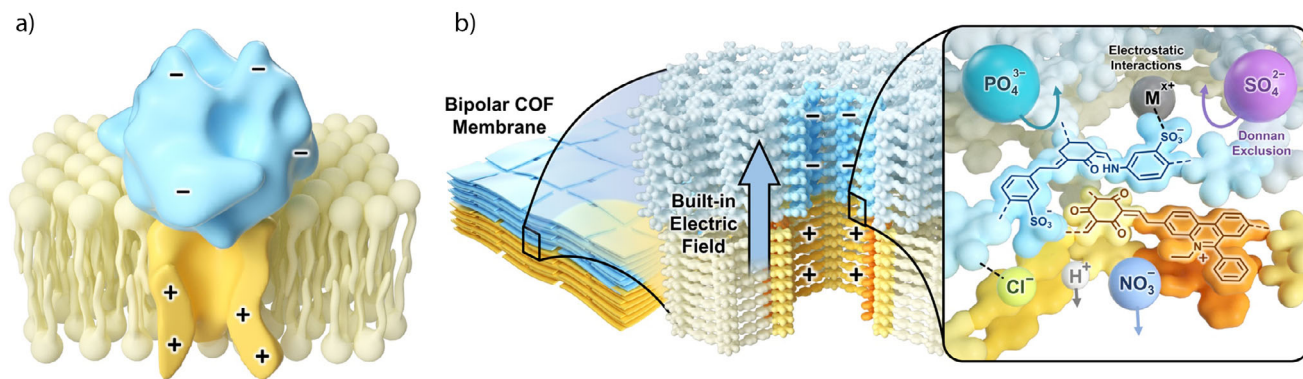


Figure 1. a) Schematic of the biological chloride channel structure for selective Cl^- transport in living organisms. b) Conceptual design of the bipolar COF membrane for HNO_3 transport.

vacuum-assisted filtration, these membranes often suffer from low operational stability and are prone to detachment from the supporting substrate.^[53]

In this study, we introduce an innovative method for fabricating bipolar COF membranes with spatially defined charge asymmetry. Our approach combines liquid–solid–liquid interfacial polymerization to synthesize ionic COF layers on porous substrates, followed by the deposition of oppositely charged COF nanosheets. By carefully controlling the ionic/non-ionic monomer ratios and colloidal nanosheet solution volumes in β -ketoenamine-linked COFs, we create membranes with well-defined charge distribution profiles, tailored short-range interaction zones around ionic sites, and enhanced ion recognition and rectification capabilities. The resulting membranes exhibit exceptional selectivity for HNO_3 (in comparison to HCl , H_2SO_4 , H_3PO_4 , and metal salts), enabling efficient HNO_3 extraction from mixed waste streams (Figure 1b). Importantly, the asymmetric charge distribution accelerates the transport of NO_3^- , achieving a transmembrane diffusion coefficient 1.44 times greater than the self-diffusion of NO_3^- . Despite an increase in membrane thickness, bipolar configurations simultaneously enhance both ionic selectivity ($175 \times$ higher than monopolar membranes) and NO_3^- flux ($1.6 \times$ increase). This work establishes a new paradigm for designing charge-asymmetry membranes with programmable ion transport properties, opening opportunities for targeted ion recovery in both environmental and industrial applications.

Results and Discussion

To validate our design strategy, we utilized triformylphloroglucinol (Tp) as the core building block for COF membrane synthesis, taking advantage of its ability to form chemically stable β -ketoenamine linkages through condensation with amine monomers.^[54] This approach not only ensures structural integrity but also facilitates short-range interactions with ions, enhancing the ion-selective capabilities of the membrane. For asymmetric charge engineering, we constructed cationic and anionic COF layers using distinct monomer pairs: Tp was coupled with ethidium bromide (EB) to generate posi-

tively charged frameworks, while 2,5-diaminobenzenesulfonic acid (SA) served as the sulfonate-functionalized monomer to induce negative charges. The fabrication process began with liquid–solid–liquid interfacial polymerization of the cationic COF layer on a polyacrylonitrile (PAN) substrate, chosen for its superior interfacial adhesion and structural stability. To systematically tune the charge density within the cationic layer, we employed a multivariate synthesis strategy. This involved co-condensation of Tp with EB and the charge-neutral monomer benzidine (BD) at controlled molar ratios, catalyzed by *p*-toluenesulfonic acid (TsOH).^[55] The resulting cationic membranes, denoted as COF-EB_x/PAN (where *x* represents the EB/(EB + BD) molar ratio), were then functionalized with anionic COF-SA nanosheets. Precise control over the thickness of the anionic layer was achieved by adjusting the deposition volume of COF-SA colloidal suspensions onto the cationic COF-EB_x/PAN layer. After deposition, thermal annealing at 70 °C was employed to induce solvent evaporation and facilitate interlayer consolidation, resulting in a mechanically robust bipolar membrane architecture (Figure 2a). The COF-SA nanosheets were synthesized through a controlled mixing protocol: Tp and SA monomers dissolved in dimethyl sulfoxide (DMSO) underwent sequential stirring and static aging (24 h, ambient conditions). A characteristic chromatic transition from red to dark red signified nanosheet formation.^[56,57] Post-synthesis purification, achieved through 3-day dialysis against deionized water, effectively removed residual monomers and oligomers (Figure S1).

Fourier Transform Infrared (FT-IR) spectroscopy of the COF-EB_x/PAN membranes demonstrated the disappearance of characteristic absorption bands associated with primary amine stretches ($3130\text{--}3330\text{ cm}^{-1}$) typical of the diamine monomer, as well as the aldehyde group stretch (1636 cm^{-1}) from Tp. The appearance of new C–N stretching bands at 1258 cm^{-1} and a ketone carbonyl stretch at 1630 cm^{-1} confirmed the extensive polymerization and the formation of β -ketoenamine linkages in the COF-EB_x/PAN structure (Figure S2).^[58] The ionic content, as measured by an electron microprobe analyzer (EMPA), indicated a bromine content in COF-EB_x/PAN ($x = 0.25$ to 1) ranging from 0.39 to 0.98 mmol g^{-1} (Table S1). Cross-sectional scanning electron

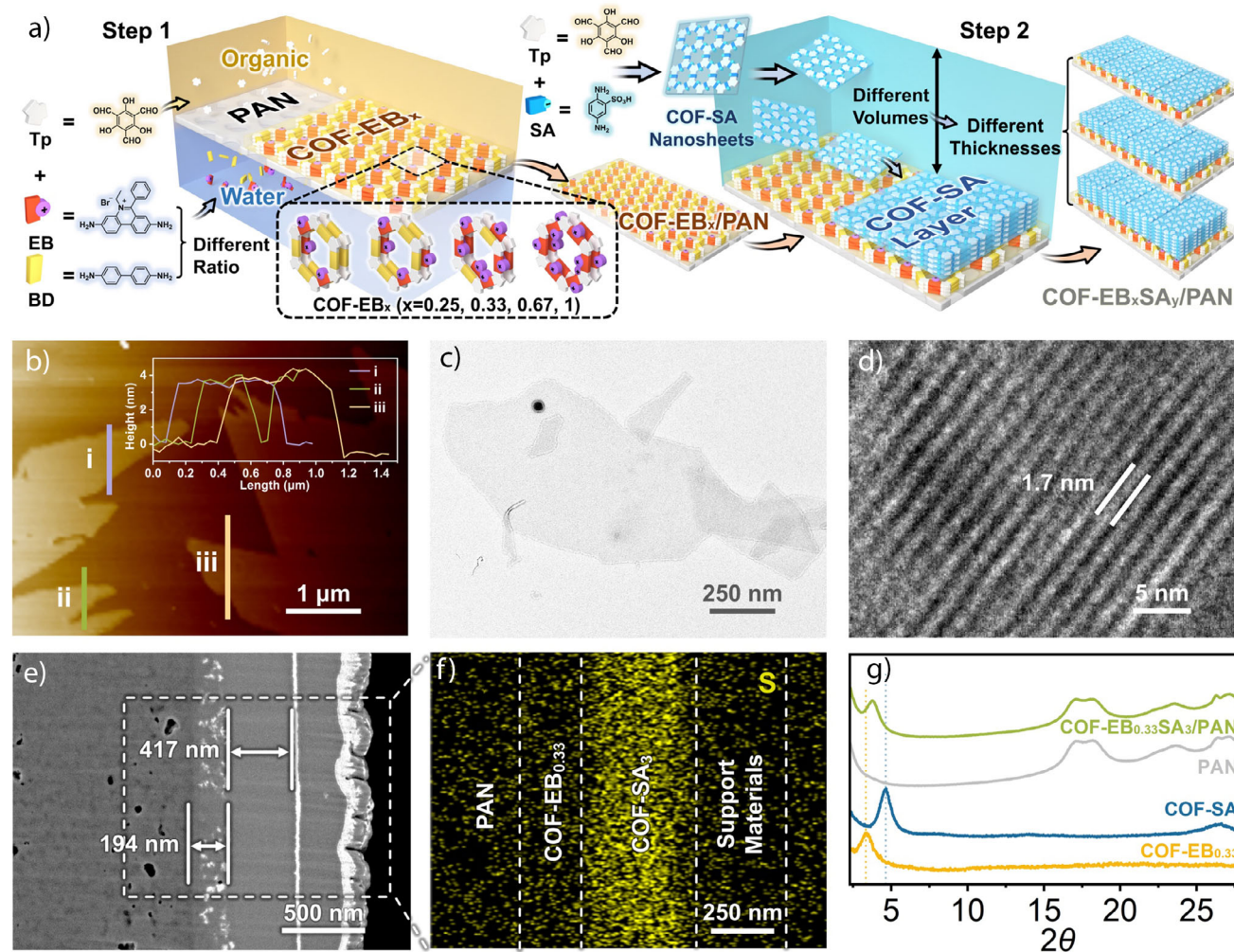


Figure 2. a) Synthetic scheme for bipolar COF-EB_xSA_y/PAN membranes. b) AFM image of COF-SA nanosheets with the inset showing height profiles; scanning areas are marked by the lines. c), d) TEM images of COF-SA nanosheets. e), f) Cross-sectional SEM image of the COF-EB_{0.33}SA₃/PAN membrane along with the corresponding EDX mapping for S element. g) WAXS analysis of COF-EB_{0.33}SA₃/PAN and PAN, as well as the PXRD pattern of free-standing COF-SA and COF-EB_{0.33}.

microscopy (SEM) images showed the membrane thickness of approximately 200 ± 20 nm, independent of the EB concentration (Figures S3–S7). Despite the thin COF layers, wide-angle X-ray scattering (WAXS) analysis exhibited distinct diffraction peaks, indicating high crystallinity (Figure S8).

In the fabrication of COF-SA nanosheets, the colloidal suspensions exhibited the Tyndall effect, suggesting the formation of nanosheets (Figure S1). Atomic force microscopy (AFM) analysis revealed a smooth, continuous surface without visible cracks or defects, indicating excellent material integrity and uniformity. Height profile measurements of the edge sections showed a consistent film thickness of approximately 4 ± 0.4 nm (Figure 2b). Transmission electron microscopy (TEM) images of drop-cast samples on ultrathin carbon films displayed a smooth, nearly transparent, flake-like morphology (Figure 2c). High-resolution TEM images further revealed distinct periodic lattice fringes with a spacing of approximately 1.7 nm (Figure 2d), characteristic of the (010) facet, confirming the superior crystallinity and porosity.

SEM images also verified the uniform flake-like morphology of the COF-SA nanosheets, while FT-IR analysis confirmed the presence of β -ketoenamine linkages in the material (Figures S9, S10). The negatively charged COF-SA colloidal suspension was then incorporated onto the positively charged COF-EB_x/PAN membranes. The atomic thickness of the COF-SA nanosheets facilitated seamless integration with the COF-EB_x/PAN membranes to form COF-EB_xSA_y/PAN, with “y” denoting the volume of COF-SA nanosheet colloidal suspensions. SEM images of the resulting bipolar COF membrane showed a dense, smooth surface, and cross-sectional views clearly revealed a bilayer structure. The thickness of the COF-SA layer was directly proportional to the volume of colloidal suspension applied. Specifically, volumes of 1, 3, and 5 mL resulted in COF-SA layer thicknesses of 170, 417, and 660 nm, respectively. Energy-dispersive X-ray (EDX) spectral mapping confirmed the presence of sulfur, indicative of the sulfonate groups in the COF layer, further supporting the formation of the bipolar membrane structure

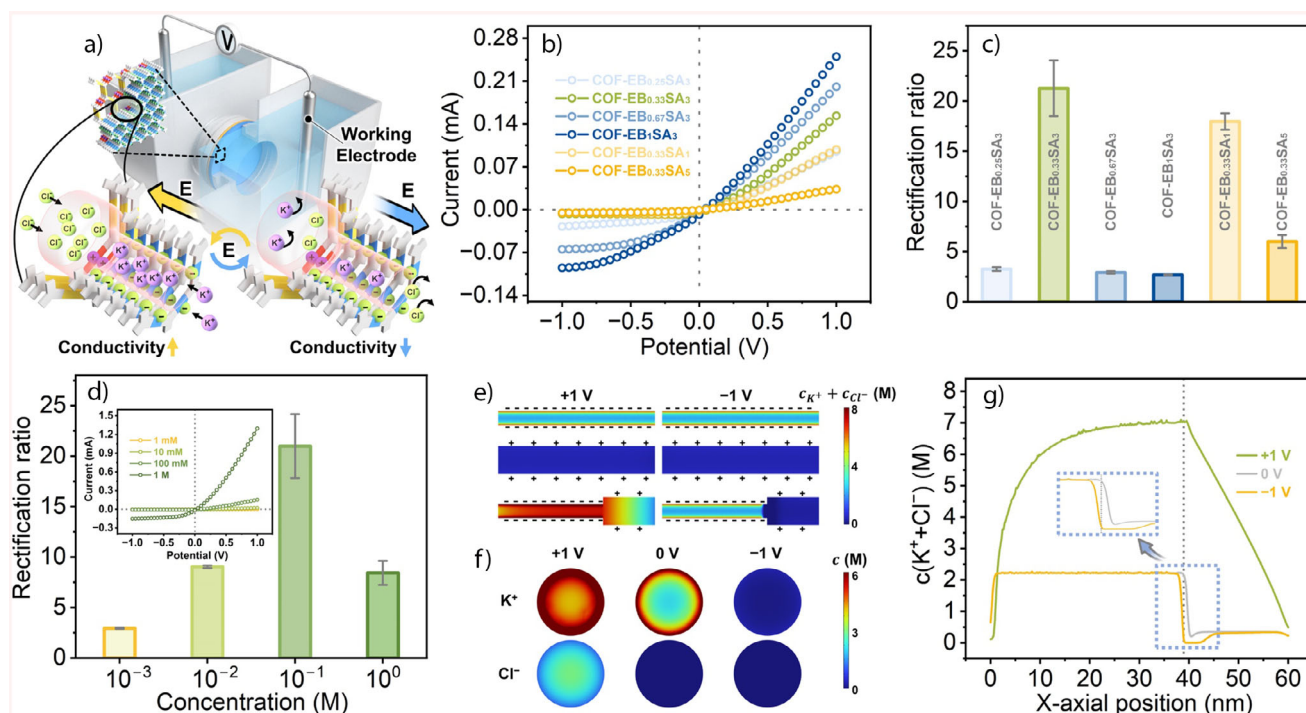


Figure 3. a) Schematic illustration of the electrochemical testing setup and ion distribution in the bipolar COF membrane channels. b), c) I - V curves of various membranes in the presence of 0.1 M KCl solution and corresponding ICR values determined as $|I_+/I_-|$ at ± 1 V. d) Effect of KCl concentration on the ICR of the COF-EB_{0.33}SA₃/PAN membrane; Inset: corresponding I - V curves. e), f) Numerical simulations of ionic concentration distribution for three models (COF-SA, COF-EB_{0.33}, and COF-EB_{0.33}SA₃, from top to bottom) and the Y - Z cross-sectional concentration images of K^+ and Cl^- at 39 nm along the X -axis under various voltages, showing that ionic rectification is induced by ion depletion and accumulation effects caused by the different polarity of the external voltage. g) Numerical simulation results for ionic concentration distribution in the COF-EB_{0.33}SA₃ channel.

(Figures 2e,f, and S11, S12). Ar^+ ion etching was performed on the COF-EB_{0.33}SA₃/PAN membrane. Initially, a distinct S signal attributed to the sulfonate groups in COF-SA was observed. After 5642s of etching, the S signal disappeared, with a concurrent appearance of the Br signal, confirming the formation of a bipolar membrane structure (Figure S13). WAXS analysis showed distinct diffraction peaks, indicative of high crystallinity, with merged peak positions from the COF-EB_{0.33} and COF-SA layers, confirming the creation of a bipolar COF membrane with dual crystal structures (Figure 2g).^[59] Moreover, the synthesized bipolar membrane demonstrated excellent mechanical, thermal, and chemical stability. Under shear stress, heating, and exposure to strong acidic solutions, the bilayer membrane remained intact. In sharp contrast, the bipolar COF membrane fabricated by nanosheet colloidal solution pressure vacuum filtration exhibited cracking and detachment (Figure S14).

To investigate the influence of charge asymmetry on ion transport dynamics, we systematically analyzed bipolar membrane structures using current-voltage (I - V) characterization (Figure 3a). The membranes were assembled in a custom electrochemical cell containing symmetric KCl solutions, chosen to minimize liquid junction potentials due to the similar mobilities of K^+ and Cl^- ions.^[60] Our results revealed that the bipolar membranes exhibited diode-like I - V characteristics, similar to the behavior observed in p-n semiconductor junctions (see the detailed explanation of the working principle

in Figure S15). Under a positive bias, ions accumulated in the pore channels, enhancing ionic conductivity. In contrast, under a negative bias, electrostatic repulsion hindered ion movement, creating an ion-depleted region that reduced ionic conductivity (Figure 3a, inset). In contrast, membranes with symmetric charge distributions, such as COF-EB_{0.33}/PAN and COF-SA₃/PAN, exhibited linear I - V curves and had a rectification ratio (ICR, defined as $|I_+/I_-|$ at ± 1 V) close to 1, indicating no preferential ion flow direction under the applied voltage (Figure S16). The observed ICR effects in the bipolar membranes were influenced by the distribution of charged sites, which depended on the EB moiety content in COF-EB_x and the thickness of the COF-SA layers. As the proportion of EB moieties in COF-EB_x increased, the ICR initially rose, then decreased. The highest rectification ratio of 21 was observed in the COF-EB_{0.33}SA₃/PAN membrane, which had an EB molar ratio of 0.33 and a COF-SA layer thickness of 417 nm. This placed it among the top membranes exhibiting charge asymmetry or gradient (Table S2). Reducing the COF-SA layer thickness to 170 nm slightly lowered the rectification ratio to 18, while increasing the thickness to 660 nm significantly reduced the ICR to 6 (Figures 3b,c). These results suggest that ion transport efficiency and rectification properties are strongly influenced by both the structural dimensions and the distribution of charge-carrying moieties (Figures S17-S20). Additionally, concentration-dependent studies showed that the ICR was

maximized at 0.1 M KCl (Figure 3d). At 1 M KCl, the ICR decreased by 59%, likely due to electric double layer (EDL) compression. At this concentration, the Debye length ($\lambda_D \approx 0.3$ nm) became subcritical relative to the nanochannel radii, reducing electrostatic gating efficiency (Table S3).^[61] This observation aligns with theoretical models predicting that maximal rectification occurs when λ_D matches the channel dimensions.

The ion rectification properties of the membranes were quantitatively analyzed using three-dimensional numerical simulations. The model consisted of two distinct segments with a total channel length of 60 nm: a 40 nm-long segment (diameter: 1.1 nm; surface charge density: -0.106 C m⁻²) representing the COF-SA layer, and a 20 nm-long segment (diameter: 2.2 nm; surface charge density: $+0.021$ C m⁻²) simulating the COF-EB_{0.33} layer (Figure S21). These parameters were derived from the relative thicknesses, charge densities, and pore sizes of the COF-EB_{0.33}SA₃/PAN membrane. For comparison, homogeneous channels of COF-SA₃ and COF-EB_{0.33} (each 60 nm in length) were simulated under identical geometric and electrostatic conditions. The simulation results revealed that individual COF-SA₃ and COF-EB_{0.33} channels exhibited stable ionic concentration profiles across varying bias polarities, without any noticeable rectification (Figure 3e). In contrast, the bipolar heterojunction configuration displayed significant rectification. At equilibrium (zero bias), the Donnan equilibrium governed the ion distribution: K⁺ ions accumulated preferentially in the negatively charged COF-SA₃ channel, while Cl⁻ ions concentrated in the positively charged COF-EB_{0.33} channel. Under positive bias, both ion species migrated into the channel, resulting in localized ion enrichment and a corresponding increase in ionic current. Conversely, under negative bias, ion depletion occurred along the COF channel, leading to a reduction in current (Figures 3f,g). This rectification behavior arises from the asymmetric charges between the two segments, which aligns with experimental observations of bias-dependent ion enrichment and depletion zones.

Given the exceptional ICR of the COF-EB_{0.33}SA₃/PAN membrane—a property linked to its enhanced built-in electric field—we further investigated its potential for ion-selective separations.^[62] Ion transport behavior was systematically evaluated across a range of electrolytes (HCl, KCl, NaCl, MgCl₂, CaCl₂, NaNO₃, Na₂SO₄, and Na₃PO₄ at concentrations of 0.05–0.5 M) through *I*-*V* characterization. The observed asymmetric *I*-*V* curves across all solutions confirmed the membrane's rectification capability, which facilitated accelerated ion transport under positive bias (Figures S22–S24). Among the chloride electrolytes, HCl exhibited the highest conductivity, with conductivity inversely correlated to the cation types (Figure 4a). At +1 V, conductance rankings followed this order: $G_{HCl} > G_{KCl} > G_{NaCl} > G_{CaCl_2} > G_{MgCl_2}$. Selectivity ratios at 0.5 M concentration for H⁺ over metal ions were as follows: 3.8 (H⁺/K⁺), 5.7 (H⁺/Na⁺), 12.3 (H⁺/Ca²⁺), and 18.6 (H⁺/Mg²⁺). Additionally, monovalent anions (Cl⁻, NO₃⁻) showed higher conductivity than multivalent anions (SO₄²⁻, PO₄³⁻), with conductivity differences increasing as the anionic charge increased (Figure 4b). The selectivity ratios for NO₃⁻ over other

anions, based on G_{NaNO_3} , G_{NaCl} , $G_{Na_2SO_4}$, and $G_{Na_3PO_4}$, were: NO₃⁻/Cl⁻ = 1.01, NO₃⁻/SO₄²⁻ = 17.4, and NO₃⁻/PO₄³⁻ = 20.5 (Figure 4c). The critical role of the bipolar architecture in ion selectivity was highlighted through comparative *I*-*V* analyses with monopolar membranes (COF-EB_{0.33}/PAN, COF-SA₃/PAN). The monopolar configurations exhibited up to 7.8 times lower selectivity, thus confirming the superior performance of the heterostructure in creating charge-asymmetric pathways for selective ion transport (Figures S25 and S26).

To systematically evaluate the ion-sieving capabilities of the COF-EB_{0.33}SA₃/PAN membrane, we conducted dialysis experiments using an H-type diffusion cell. The membrane separated the cell into two chambers: a feed chamber containing 20 mL electrolyte solution (0.05–0.5 M) and a permeate chamber filled with 20 mL deionized water. Ion transport dynamics were quantified by tracking time-dependent conductivity changes in the permeate chamber. Ion accumulation in the permeate chamber correlated linearly with both feed concentration and dialysis duration (Figures S27–S30). HNO₃ exhibited the highest permeance among tested electrolytes, with selectivity ratios relative to HCl, H₂SO₄, and H₃PO₄ reaching 2.1, 30.7, and 169.4, respectively, at 0.5 M. Furthermore, the selectivity ratios of H⁺ over other cations such as K⁺, Na⁺, Li⁺, Mg²⁺, and Al³⁺ were approximately 109, 135, 138, 748, and 17,126, respectively (Figure 5a). The higher selectivity for NO₃⁻ over SO₄²⁻ and PO₄³⁻ can be attributed to the Donnan exclusion mechanism, facilitated by the COF-SA layer, in combination with strong ion-dipole interactions within the β -ketoenamine linkages of the COF channels, which effectively retain higher-valent anions. Despite both NO₃⁻ and Cl⁻ ions carrying the same charge, NO₃⁻ exhibited a lower binding affinity for the membrane framework due to its more dispersed charge distribution, in contrast to the localized charge of Cl⁻ ions (Figure S31). The observed selectivity for protons over other cations may also be influenced by sub-nanoscale pore channels formed by lattice overlaps between COF-SA and COF-EB_{0.33}, as evidenced by the decreasing ion permeation rates with increasing hydrated ion diameters (Figures S32, S33).

To further assess the practical application of ion separation, particularly for recovering target species from complex solutions with competing interactions, we performed permeability measurements in the presence of multiple electrolytes. Given the challenges associated with anion separation, we tested the membrane performance using equimolar solutions of HNO₃, HCl, H₂SO₄, and H₃PO₄ at concentrations of 0.05 and 0.25 M (Figure S34). The results showed that HNO₃ consistently exhibited the highest transport rates, with selectivity ratios of HNO₃/HCl, HNO₃/H₂SO₄, and HNO₃/H₃PO₄ being 6.0, 103, and 595, respectively, after 5 h at an initial concentration of 0.05 M for each acid. When the concentration increased to 0.25 M, the selectivity ratios of HNO₃ over HCl and H₃PO₄ rose to 6.8 and 963, respectively, while the ratio over H₂SO₄ slightly decreased to 90 (Figure 5b). In the multi-acid system, the selectivity of HNO₃ compared to the other acids was significantly enhanced compared to the single-acid system. Specifically, the HNO₃/HCl and HNO₃/H₂SO₄ ratios tripled, and the HNO₃/H₃PO₄ ratio increased sixfold, highlighting the

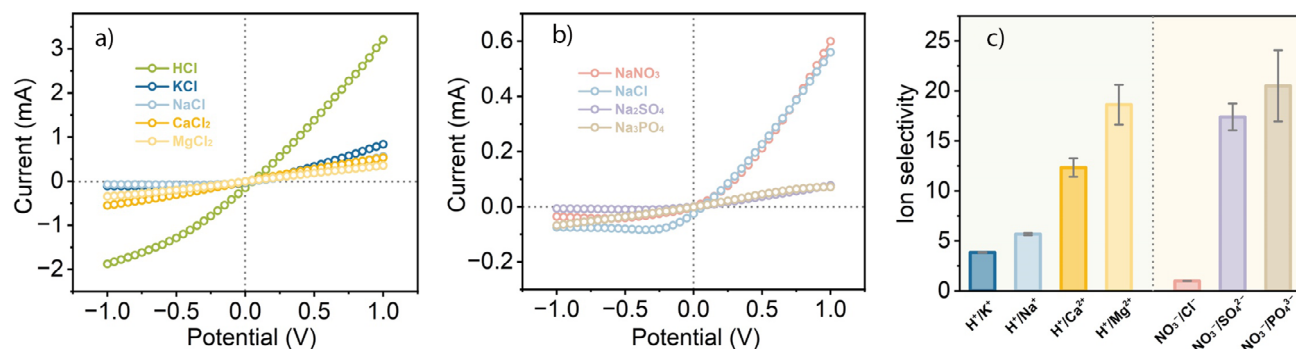


Figure 4. a), b) *I*-*V* curves of various Cl⁻ electrolytes and sodium salts across the COF-EB_{0.33}SA₃/PAN membrane tested in 0.5 M solutions. c) Corresponding ion selectivity.

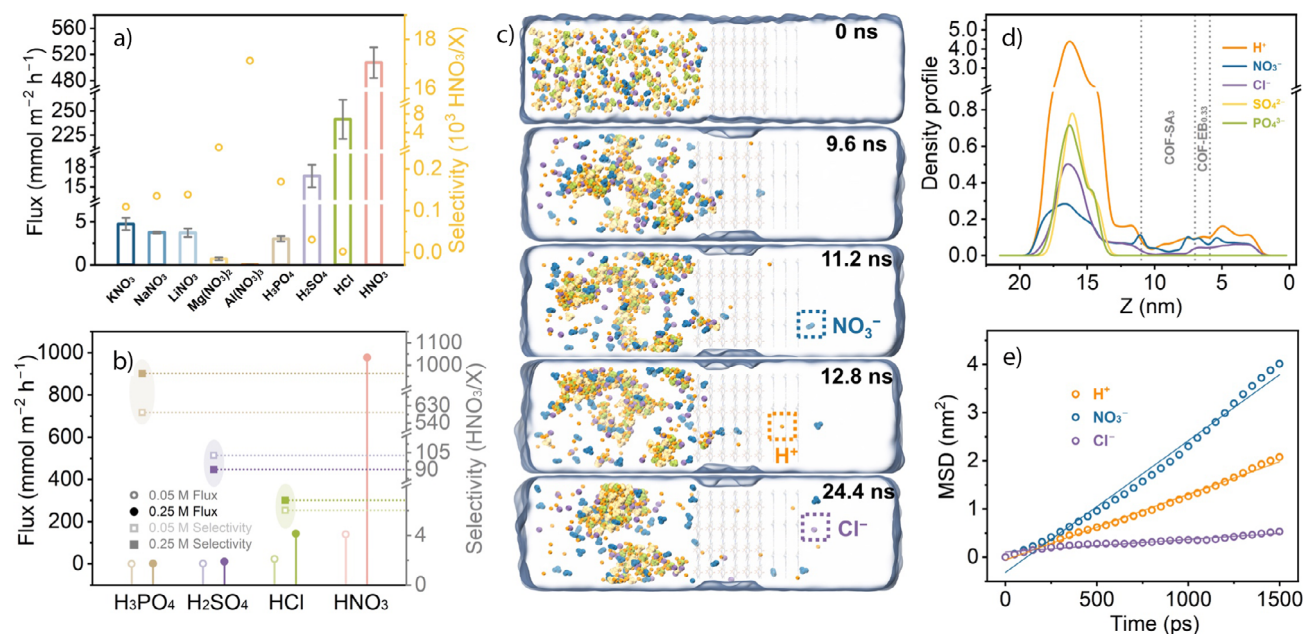


Figure 5. a) Flux of various electrolytes across the COF-EB_{0.33}SA₃/PAN membrane tested under 0.5 M single-salt conditions, with corresponding selectivity of HNO₃ over other electrolytes. b) Flux of various acids across the COF-EB_{0.33}SA₃/PAN membrane tested under multi-acid conditions, with corresponding selectivity of HNO₃ over other acids. c) Simulation snapshots depicting the transmembrane behavior of H⁺, NO₃⁻, Cl⁻, SO₄²⁻, and PO₄³⁻ (grey: COF layers, orange: H⁺, blue: NO₃⁻, purple: Cl⁻, yellow: SO₄²⁻ and green: PO₄³⁻). d) Ion density profiles along the Z - axis in different COF layers, with grey dashed lines indicating the membrane boundaries. e) Transmembrane diffusion coefficients of H⁺, NO₃⁻, and Cl⁻ ions across the COF-EB_{0.33}SA₃/PAN membrane.

interdependent nature of ion fluxes in such systems. Notably, in addition to the increased selectivity, the flux of HNO₃ also increased in the multicomponent system. At a concentration of 0.05 M, the flux of HNO₃ was 0.059 mol m⁻² h⁻¹ under single-acid conditions and 0.139 mol m⁻² h⁻¹ in the four-component system. This difference became even more pronounced at 0.25 M, with flux rates of 0.27 mol m⁻² h⁻¹ under single-acid conditions and 0.98 mol m⁻² h⁻¹ in the multicomponent system, outperforming most of the reported systems (Table S4). Despite their greater thickness, COF-EB_{0.33}SA₃/PAN membranes outperformed the individual counterparts (COF-SA₃/PAN and COF-EB_{0.33}/PAN), delivering flux rates up to 1.6 times higher and selectivity ratios up to 175 times greater (Figures S35–S37). Furthermore, the COF-EB_{0.33}SA₃/PAN membrane demonstrated excellent

stability under highly acidic conditions, as evidenced by the retention of its chemical structure, morphology, and crystallinity, confirmed through FT-IR, SEM, and WAXS analyses (Figures S38–S40).

To elucidate the molecular mechanisms of ion transport, we performed molecular dynamics (MD) simulations on a system containing HNO₃, HCl, H₂SO₄, and H₃PO₄, each at a concentration of 0.25 M, to analyze the permeation behaviors of different anions (Figure S41). Our trajectory data revealed that NO₃⁻ ions penetrated and traversed the membrane pores more rapidly than Cl⁻ ions, while SO₄²⁻ and PO₄³⁻ ions were almost entirely excluded (Figure 5c). Notably, despite the higher concentration of H⁺ ions, NO₃⁻ ions exhibited a significantly faster translocation rate. A detailed analysis of the simulation trajectory between 140 and 160 ns revealed

distinct concentration peaks for SO_4^{2-} and PO_4^{3-} on the feed side of the COF membrane, whereas NO_3^- , Cl^- , and H^+ ions were predominantly located on the membrane and permeate sides, indicating more effective transmembrane transport. Moreover, the number of NO_3^- ions crossing the membrane was substantially greater than that of Cl^- ions within the same time frame (Figure S4d). These observations correlate with their transmembrane diffusion coefficients, which were measured as $2.74 \times 10^{-5} \text{ cm}^2 \text{ s}^{-1}$ for NO_3^- , $1.36 \times 10^{-5} \text{ cm}^2 \text{ s}^{-1}$ for H^+ , $2.57 \times 10^{-6} \text{ cm}^2 \text{ s}^{-1}$ for Cl^- , and 0 for SO_4^{2-} and PO_4^{3-} , respectively (Figure S4e). Conversely, the self-diffusion coefficients for NO_3^- , H^+ , and Cl^- ions were recorded at 1.90×10^{-5} , 9.31×10^{-5} , and $2.03 \times 10^{-5} \text{ cm}^2 \text{ s}^{-1}$,^[63] respectively, which indicates the transmembrane transport rate of NO_3^- far exceeded its self-diffusion rate, while the transmembrane diffusion coefficients for H^+ and Cl^- were only about 1/6.84 and 1/7.90 of their respective free diffusion rates. Hence, the order of ion transport efficiency across the membrane was $\text{NO}_3^- > \text{H}^+ > \text{Cl}^- \gg \text{SO}_4^{2-}, \text{PO}_4^{3-}$. We attribute the enhanced transmembrane diffusion of NO_3^- to the unique bipolar structure of the membrane, which creates an intrinsic electric field across the membrane. This electric field significantly enhances the transport of NO_3^- , which has the lowest charge density among the tested anions, and thus experiences minimal Donnan repulsion. To further substantiate this observation, we calculated the transmembrane diffusion coefficients of these ions in the COF-SA membrane (Figure S42). Simulation snapshots revealed that H^+ ions penetrated and traversed the membrane pores more rapidly than NO_3^- and Cl^- ions, while SO_4^{2-} and PO_4^{3-} ions were also nearly completely excluded (Figure S43). The results confirmed that the diffusion coefficient of NO_3^- was lower than that of H^+ and also lower than its free diffusion coefficient in solution, leading to transmembrane diffusion coefficients of $1.05 \times 10^{-5} \text{ cm}^2 \text{ s}^{-1}$ for H^+ , $4.36 \times 10^{-6} \text{ cm}^2 \text{ s}^{-1}$ for NO_3^- , and $1.45 \times 10^{-6} \text{ cm}^2 \text{ s}^{-1}$ for Cl^- (Figure S44). Furthermore, the potentials of mean force (PMF) profiles for NO_3^- ions translocating through the COF-EB_{0.33}SA₃ channels showed a declining curve, indicating that NO_3^- ions encounter lower resistance when diffusing through the channel compared to their free diffusion in solution. In contrast, the PMF profiles for NO_3^- ions in the COF-SA channels exhibited an increasing trend, which is consistent with the observed diffusion coefficient trends (Figure S45).

To explain the enhanced ion flux observed in multicomponent acid systems compared to single-acid conditions for the bipolar COF-EB_{0.33}SA₃/PAN membrane, we propose a synergistic mechanism involving competitive ion transport modulation and charge-density-dependent exclusion effects. The high ionic concentration gradient in mixed-acid systems promotes ion accumulation within the membrane's nanochannels, reducing transmembrane resistance and accelerating ion permeation. Strong Donnan repulsion from the COF-SA layer effectively excludes multivalent anions (such as SO_4^{2-} and PO_4^{3-}), while stronger binding interactions with Cl^- prevent its transport. In contrast, the weakest electrostatic interactions allow preferential translocation of NO_3^- , providing a competitive diffusion advantage for HNO_3 over other acids. The exceptional selectivity of $\text{HNO}_3/\text{H}_3\text{PO}_4$ (up

to 963 at 0.25 M) is attributed to acid speciation effects. The increased H^+ concentration suppresses the dissociation of H_3PO_4 , thereby reducing the concentration of PO_4^{3-} in the system. This hierarchical sieving mechanism, which integrates charge asymmetry, pore chemistry, and acid-base equilibria, accounts for the membrane outstanding selectivity for HNO_3 recovery from complex acidic mixtures.

Encouraged by these findings, we further explored the ability of COF-EB_{0.33}SA₃/PAN to selectively separate HNO_3 from a complex mixture containing various ions, including Li^+ , Na^+ , K^+ , Mg^{2+} , Cl^- , SO_4^{2-} , and PO_4^{3-} . This investigation aimed to assess its potential for extracting HNO_3 from mixed waste streams. The performance of the membrane was evaluated in terms of the flux and selectivity of HNO_3 , HCl , H_2SO_4 , H_3PO_4 , LiNO_3 , NaNO_3 , KNO_3 , and $\text{Mg}(\text{NO}_3)_2$, each at an equimolar concentration of 0.1 M, over time (Figure S46). The results demonstrated that the COF-EB_{0.33}SA₃/PAN membrane consistently exhibited high selectivity ratios for HNO_3 over HCl , H_2SO_4 , and H_3PO_4 , with values of 22, 252, and 500, respectively. Notably, the ratios of HNO_3 to other metal nitrates varied significantly, ranging from 322 to 242,000. These findings underscore the unique potential of bipolar COF membranes to extract valuable chemicals from complex contaminant mixtures. Furthermore, the performance of the HNO_3 extraction in terms of purity and flux remained stable, with a slight initial increase during the first 90 h, followed by a sustained level for at least 257 h. Notably, after a single pass through the membrane, the purity of HNO_3 increased from 12.5% to 94.1% (Figures 6a,b).

To further evaluate the long-term stability under harsh acidic conditions, we compared the COF-EB_{0.33}SA₃/PAN membrane with the commercial DF-120 membrane, which serves as a state-of-the-art benchmark for acid dialysis.^[64,65] The testing involved a 5-component acidic mixture consisting of 0.5 M each of HNO_3 , HCl , H_2SO_4 , H_3PO_4 , and $\text{Mg}(\text{NO}_3)_2$, resulting in a total H^+ concentration of 3.5 M. Due to the low flux rates of Mg^{2+} and PO_4^{3-} , data collection began after 25 h. After 53.5 h, the COF-EB_{0.33}SA₃/PAN membrane retained 88%–95% of its initial selectivity compared to its baseline value at 25 h. The selectivity of NO_3^- over other anions was 18 (vs. Cl^-), 327 (vs. PO_4^{3-}), 213 (vs. SO_4^{2-}), and the selectivity of H^+ over Mg^{2+} reached 58404. In contrast, the DF-120 membrane exhibited a significant performance decline, retaining only 78%–93% of its initial selectivity. The selectivity of NO_3^- over other ions was 6 (vs. Cl^-), 29 (vs. PO_4^{3-}), 14 (vs. SO_4^{2-}), and the selectivity of H^+ over Mg^{2+} was 1853. Both membranes showed a gradual decrease in HNO_3 flux over time. The flux of COF-EB_{0.33}SA₃/PAN decreased from $1.5 \text{ mol m}^{-2} \text{ h}^{-1}$ at 25 h to $1.3 \text{ mol m}^{-2} \text{ h}^{-1}$ at 53.5 h, while the flux of DF-120 decreased from $3.0 \text{ mol m}^{-2} \text{ h}^{-1}$ at 25 h to $2.5 \text{ mol m}^{-2} \text{ h}^{-1}$ at 53.5 h. Importantly, the performance of COF-EB_{0.33}SA₃/PAN was fully restored after a brief washing step, while the DF-120 membrane only recovered 76% of its initial $\text{H}^+/\text{Mg}^{2+}$ separation efficiency compared to the value at 25 h (Figure S47). Therefore, we attribute the decrease in HNO_3 flux for COF-EB_{0.33}SA₃/PAN to concentration polarization. Post-test SEM and FT-IR analyses confirmed that the bipolar COF membrane showed no

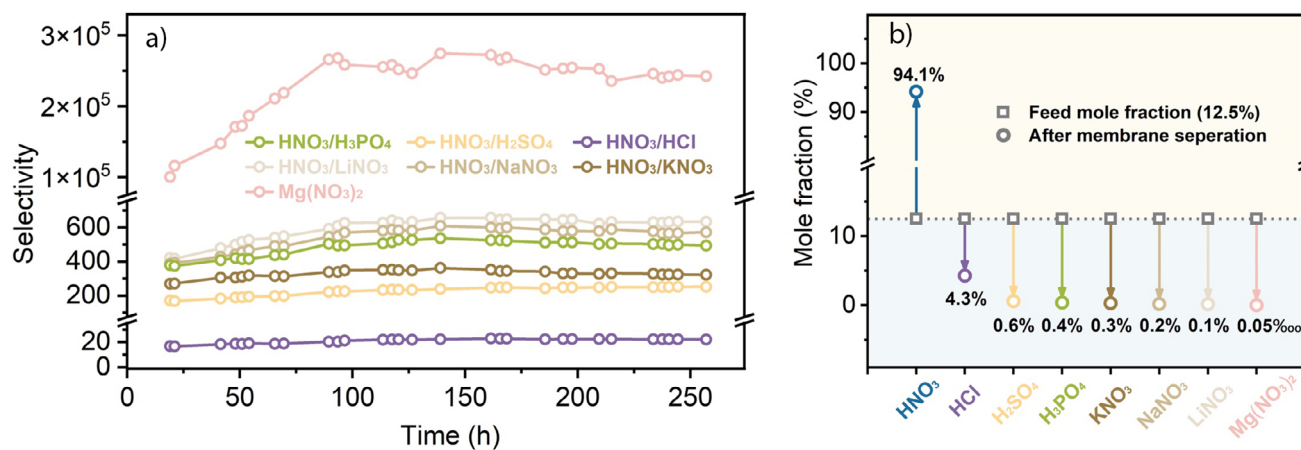


Figure 6. a) Selectivity of HNO₃ over other electrolytes in the extraction from mixed waste streams (0.1 M each). b) Ion composition of the waste stream pre- and post-membrane separation, assessed over a testing period of 257 h.

signs of structural or chemical degradation, whereas the DF-120 membrane displayed clear FT-IR spectral changes after use. These results demonstrate the exceptional stability and durability of our membrane under strong acidic conditions (Figures S48, S49).

Conclusion

In summary, we have successfully developed a straightforward method for constructing bipolar COF membranes with customizable distributions of ionic sites. This is achieved by casting ionic COF nanosheet colloidal suspensions onto COF layers of the opposite charge polarity. The resultant membranes demonstrate exceptional selectivity, distinguishing between protons and metal ions and differentiating NO₃⁻ from other anions, achieving selectivity values as high as 242000 and 963, respectively. This performance represents up to a 175-fold improvement over the corresponding positively or negatively charged COF membranes. The distinct bipolar membrane architecture not only enhances the selectivity for HNO₃ over other solutes but also significantly increases the flux of HNO₃. This is attributed to the intrinsic built-in electric field within the membrane, which facilitates efficient NO₃⁻ transport, as evidenced by a transmembrane diffusion coefficient that surpasses the self-diffusion value. This, in turn, boosts separation efficiency compared to competing ion transport processes. Given the modularity of COF chemistry and the scalability of our fabrication approach, this platform enables rational engineering of membranes for demanding separations, including industrial acid recovery and environmental remediation. Future integration of bioinspired motifs (e.g., proton-relay networks, gated pores) could bridge the performance gap between synthetic and biological ion channels, advancing toward atomically precise separations.

Acknowledgements

This work is supported by the National Key Research and Development Program of China (2024YFB3815700), the

National Natural Science Foundation of China (22421004), and the National Natural Science Foundation of Zhejiang Province (LR23B060001). We sincerely thank Ms. Fang Chen from the Analysis and Test Platform, Department of Chemistry, Zhejiang University, for her assistance with membrane ion milling treatment and EDX analysis.

Conflict of Interests

The authors declare no conflict of interest.

Data Availability Statement

The data that support the findings of this study are available in the supplementary material of this article.

Keywords: Bipolar membrane • Charge manipulation • Covalent organic framework membrane • Ion rectification • Single-acid recovery

- [1] Z. Wang, L. Huang, X. Dong, T. Wu, Q. Qing, J. Chen, Y. Lu, C. Xu, *Nat. Commun.* **2023**, *14*, 261.
- [2] Q. Lu, Y. Ma, H. Li, X. Guan, Y. Yusran, M. Xue, Q. Fang, Y. Yan, S. Qiu, V. Valtchev, *Angew. Chem. Int. Ed.* **2018**, *57*, 6042–6048.
- [3] L. Xu, W. Liu, X. Zhang, W. Tang, D.-J. Lee, Z. Yang, Z. Chen, S. Lin, *Nat. Water* **2024**, *2*, 999–1008.
- [4] D. Zhang, T. K. Ronson, J. Mosquera, A. Martinez, J. R. Nitschke, *Angew. Chem. Int. Ed.* **2018**, *57*, 3717–3721.
- [5] D. S. Sholl, R. P. Lively, *Nature* **2016**, *532*, 435–437.
- [6] Q. Sun, B. Aguila, Y. Song, S. Ma, *Acc. Chem. Res.* **2020**, *53*, 812–821.
- [7] Z. Lu, Y. Wu, L. Ding, Y. Wei, H. Wang, *Angew. Chem. Int. Ed.* **2021**, *60*, 22265–22269.
- [8] A. Iddya, P. Zarzycki, R. Kingsbury, C. M. Khor, S. Ma, J. Wang, I. Wheeldon, Z. J. Ren, E. M. V. Hoek, D. Jassby, *Nat. Nanotechnol.* **2022**, *17*, 1222–1228.
- [9] W. Xin, J. Fu, Y. Qian, L. Fu, X.-Y. Kong, T. Ben, L. Jiang, L. Wen, *Nat. Commun.* **2022**, *13*, 1701.

- [10] X. Ruan, C. Zhang, Y. Zhu, F. Cai, Y. Yang, J. Feng, X. Ma, Y. Zheng, H. Li, Y. Yuan, G. Zhu, *Angew. Chem. Int. Ed.* **2023**, *62*, e202216549.
- [11] M. Zhang, K. Guan, Y. Ji, G. Liu, W. Jin, N. Xu, *Nat. Commun.* **2019**, *10*, 1253.
- [12] Q. Li, H. Gao, Y. Zhao, B. Zhou, L. Yu, Q. Huang, L. Jiang, J. Gao, *Angew. Chem. Int. Ed.* **2024**, *63*, e202402094.
- [13] Q. Liu, M. Liu, Z. Zhang, C. Yin, J. Long, M. Wei, Y. Wang, *Nat. Commun.* **2024**, *15*, 9221.
- [14] R. M. DuChanois, M. Heiranian, J. Yang, C. J. Porter, Q. Li, X. Zhang, R. Verduzco, M. Elimelech, *Sci. Adv.* **2022**, *8*, eabm9436.
- [15] C. Zhao, J. Hou, M. Hill, B. Freeman, H. Wang, H. Zhang, *Acc. Mater. Res.* **2023**, *4*, 786–797.
- [16] Q.-W. Meng, S. Wu, M. Liu, Q. Guo, W. Xian, X. Zuo, S. Wang, H. Yin, S. Ma, Q. Sun, *Sci. Adv.* **2023**, *9*, eadh0207.
- [17] R. Tan, A. Wang, R. Malpass-Evans, R. Williams, E. W. Zhao, T. Liu, C. Ye, X. Zhou, B. P. Darwich, Z. Fan, L. Turcani, E. Jackson, L. Chen, S. Y. Chong, T. Li, K. E. Jelfs, A. I. Cooper, N. P. Brandon, C. P. Grey, N. B. McKeown, Q. Song, *Nat. Mater.* **2020**, *19*, 195–202.
- [18] Y. Li, Q. Wu, X. Guo, M. Zhang, B. Chen, G. Wei, X. Li, X. Li, S. Li, L. Ma, *Nat. Commun.* **2020**, *11*, 599.
- [19] P. Zuo, C. Ye, Z. Jiao, J. Luo, J. Fang, U. S. Schubert, N. B. McKeown, T. L. Liu, Z. Yang, T. Xu, *Nature* **2023**, *617*, 299–305.
- [20] R. Xu, Y. Kang, W. Zhang, X. Zhang, B. Pan, *Angew. Chem. Int. Ed.* **2022**, *61*, e202115443.
- [21] S. Hong, M. Di Vincenzo, A. Tiraferri, E. Bertozzi, R. Górecki, B. Davaasuren, X. Li, S. P. Nunes, *Nat. Commun.* **2024**, *15*, 3160.
- [22] H. Yang, J. Xu, H. Cao, J. Wu, D. Zhao, *Nat. Commun.* **2023**, *14*, 2726.
- [23] R.-J. Mo, S. Chen, L.-Q. Huang, X.-L. Ding, S. Rafique, X.-H. Xia, Z.-Q. Li, *Nat. Commun.* **2024**, *15*, 2145.
- [24] X. Li, H. Zhang, J. Hou, R. Ou, Y. Zhu, C. Zhao, T. Qian, C. D. Easton, C. Selomulya, M. R. Hill, H. Wang, *J. Am. Chem. Soc.* **2020**, *142*, 9827–9833.
- [25] L. Cao, I.-C. Chen, Z. Li, X. Liu, M. Mubashir, R. A. Nuaimi, Z. Lai, *Nat. Commun.* **2022**, *13*, 7894.
- [26] C. Violet, A. Ball, M. Heiranian, L. F. Villalobos, J. Zhang, B. Uralcan, H. Kulik, A. Haji-Akbari, M. Elimelech, *Nat. Water* **2024**, *2*, 706–718.
- [27] C. Wang, M. M. Polovitskaya, B. D. Delgado, T. J. Jentsch, S. B. Long, *Sci. Adv.* **2022**, *8*, eabm3942.
- [28] D. A. Köpfer, C. Song, T. Gruene, G. M. Sheldrick, U. Zachariae, B. L. De Groot, *Science* **2014**, *346*, 352–355.
- [29] S. Zheng, L. Huang, Z. Sun, M. Barboiu, *Angew. Chem. Int. Ed.* **2021**, *60*, 566–597.
- [30] Z. Ruan, J. Osei-Owusu, J. Du, Z. Qiu, W. Lü, *Nature* **2020**, *588*, 350–354.
- [31] K. Xiao, L. Chen, Z. Zhang, G. Xie, P. Li, X.-Y. Kong, L. Wen, L. Jiang, *Angew. Chem. Int. Ed.* **2017**, *56*, 8168–8172.
- [32] L. Ding, M. Zheng, D. Xiao, Z. Zhao, J. Xue, S. Zhang, J. Caro, H. Wang, *Angew. Chem. Int. Ed.* **2022**, *61*, e202206152.
- [33] Z. Siwy, E. Heins, C. C. Harrell, P. Kohli, C. R. Martin, *J. Am. Chem. Soc.* **2004**, *126*, 10850–10851.
- [34] C. Li, L. Wen, X. Sui, Y. Cheng, L. Gao, L. Jiang, *Sci. Adv.* **2021**, *7*, eabg2183.
- [35] L.-J. Cheng, L. J. Guo, *Chem. Soc. Rev.* **2010**, *39*, 923–938.
- [36] Z. Zhang, X. Sui, P. Li, G. Xie, X.-Y. Kong, K. Xiao, L. Gao, L. Wen, L. Jiang, *J. Am. Chem. Soc.* **2017**, *139*, 8905–8914.
- [37] M. B. Asif, S. Kim, T. S. Nguyen, J. Mahmood, C. T. Yavuz, *J. Am. Chem. Soc.* **2024**, *146*, 3567–3584.
- [38] K. Geng, T. He, R. Liu, S. Dalapati, K. T. Tan, Z. Li, S. Tao, Y. Gong, Q. Jiang, D. Jiang, *Chem. Rev.* **2020**, *120*, 8814–8933.
- [39] Y. Yang, B. Liang, J. Kreie, M. Hamsch, Z. Liang, C. Wang, S. Huang, X. Dong, L. Gong, C. Liang, D. Lou, Z. Zhou, J. Lu, Y. Yang, X. Zhuang, H. Qi, U. Kaiser, S. C. B. Mannsfeld, W. Liu, A. Götzhäuser, Z. Zheng, *Nature* **2024**, *630*, 878–883.
- [40] G. He, R. Zhang, Z. Jiang, *Acc. Mater. Res.* **2021**, *2*, 630–643.
- [41] J. Han, J. Feng, J. Kang, J.-M. Chen, X.-Y. Du, S.-Y. Ding, L. Liang, W. Wang, *Science* **2024**, *383*, 1014–1019.
- [42] B. Hou, K. Wang, C. Jiang, Y. Guo, X. Zhang, Y. Liu, Y. Cui, *Angew. Chem. Int. Ed.* **2024**, *63*, e202412380.
- [43] S. Zhao, C. Jiang, J. Fan, S. Hong, P. Mei, R. Yao, Y. Liu, S. Zhang, H. Li, H. Zhang, C. Sun, Z. Guo, P. Shao, Y. Zhu, J. Zhang, L. Guo, Y. Ma, J. Zhang, X. Feng, F. Wang, H. Wu, B. Wang, *Nat. Mater.* **2021**, *20*, 1551–1558.
- [44] L. Li, Q. Yun, C. Zhu, G. Sheng, J. Guo, B. Chen, M. Zhao, Z. Zhang, Z. Lai, X. Zhang, Y. Peng, Y. Zhu, H. Zhang, *J. Am. Chem. Soc.* **2022**, *144*, 6475–6482.
- [45] Y. Kong, B. Lyu, C. Fan, Y. Yang, X. Wang, B. Shi, J. Jiang, H. Wu, Z. Jiang, *J. Am. Chem. Soc.* **2023**, *145*, 27984–27992.
- [46] S. Wang, Y. Fu, F. Wang, X. Wang, Y. Yang, M. Wang, J. Wang, E. Lin, H. Ma, Y. Chen, P. Cheng, Z. Zhang, *J. Am. Chem. Soc.* **2024**, *146*, 33509–33517.
- [47] C. S. Diercks, O. M. Yaghi, *Science* **2017**, *355*, eaal1585.
- [48] Y. Yin, Y. Zhang, X. Zhou, B. Gui, W. Wang, W. Jiang, Y.-B. Zhang, J. Sun, C. Wang, *Science* **2024**, *386*, 693–696.
- [49] S. Yin, J. Li, Z. Lai, Q.-W. Meng, W. Xian, Z. Dai, S. Wang, L. Zhang, Y. Xiong, S. Ma, Q. Sun, *Nat. Commun.* **2024**, *15*, 8137.
- [50] K. H. Sippel, F. A. Quioco, *Protein Sci.* **2015**, *24*, 1040–1046.
- [51] Z. Mu, Y. Zhu, Y. Zhang, A. Dong, C. Xing, Z. Niu, B. Wang, X. Feng, *Angew. Chem. Int. Ed.* **2023**, *62*, e202300373.
- [52] Z.-B. Zhou, P.-J. Tian, J. Yao, Y. Lu, Q.-Y. Qi, X. Zhao, *Nat. Commun.* **2022**, *13*, 2180.
- [53] M. Wang, P. Zhang, X. Liang, J. Zhao, Y. Liu, Y. Cao, H. Wang, Y. Chen, Z. Zhang, F. Pan, Z. Zhang, Z. Jiang, *Nat. Sustain.* **2022**, *5*, 518–526.
- [54] S. Kandambeth, A. Mallick, B. Lukose, M. V. Mane, T. Heine, R. Banerjee, *J. Am. Chem. Soc.* **2012**, *134*, 19524–19527.
- [55] L. Hou, W. Xian, S. Bing, Y. Song, Q. Sun, L. Zhang, S. Ma, *Adv. Funct. Mater.* **2021**, *31*, 2009970.
- [56] T. Huang, H. Jiang, J. C. Douglin, Y. Chen, S. Yin, J. Zhang, X. Deng, H. Wu, Y. Yin, D. R. Dekel, M. D. Guiver, Z. Jiang, *Angew. Chem. Int. Ed.* **2023**, *62*, e202209306.
- [57] K. Koner, H. S. Sasmal, D. Shetty, R. Banerjee, *Angew. Chem. Int. Ed.* **2024**, *63*, e202406418.
- [58] W. Xian, X. Zuo, C. Zhu, Q. Guo, Q.-W. Meng, X. Zhu, S. Wang, S. Ma, Q. Sun, *Nat. Commun.* **2022**, *13*, 3386.
- [59] B.-B. Luan, X. Chu, Y. Wang, X. Qiao, Y. Jiang, F.-M. Zhang, *Adv. Mater.* **2024**, *36*, 2412653.
- [60] W. Xian, X. Xu, Y. Ge, Z. Xing, Z. Lai, Q.-W. Meng, Z. Dai, S. Wang, R. Chen, N. Huang, S. Ma, Q. Sun, *J. Am. Chem. Soc.* **2024**, *146*, 33973–33982.
- [61] L. Bocquet, E. Charlaix, *Chem. Soc. Rev.* **2010**, *39*, 1073–1095.
- [62] X. Zhu, J. Hao, B. Bao, Y. Zhou, H. Zhang, J. Pang, Z. Jiang, L. Jiang, *Sci. Adv.* **2018**, *4*, eaau1665.
- [63] Q. Liu, Y. Wang, W. Guo, H. Ji, J. Xue, Q. Ouyang, *Phys. Rev. E* **2007**, *75*, 051201.
- [64] X. Li, J. Gu, Z. Hong, Z. Shen, Z. Ji, R. Tan, R. Jia, J. Yang, S. Zhang, Z. Wan, J. Ran, P. Zuo, *J. Membr. Sci.* **2025**, *722*, 123910.
- [65] J. Lin, X. Dan, J. Wang, S. Huang, L. Fan, M. Xie, S. Zhao, X. Lin, *J. Membr. Sci.* **2023**, *673*, 121499.

Manuscript received: February 17, 2025

Revised manuscript received: April 26, 2025

Accepted manuscript online: April 28, 2025

Version of record online: May 05, 2025